IOP Publishing | International Atomic Energy Agency Nuclear Fusion

Nucl. Fusion **59** (2019) 046005 (12pp) https://doi.org/10.1088/1741-4326/aafe3a

# Effects of RMP-induced changes of radial electric fields on microturbulence in DIII-D pedestal top

**S. Taimourzadeh**[1], **L. Shi**[1], **Z. Lin**[1], **R. Nazikian**[2], **I. Holod**[1,3] **and D. Spong**[4]

[1] Department of Physics and Astronomy, University of California, Irvine, CA 92697, United States of America
[2] Princeton Plasma Physics Laboratory, Princeton, NJ 08543, United States of America
[3] Lawrence Livermore National Laboratory, Livermore, CA 94550, United States of America
[4] Oak Ridge National Laboratory, Oak Ridge, TN 37831, United States of America

E-mail: zhihongl@uci.edu

Received 2 September 2018, revised 22 December 2018
Accepted for publication 14 January 2019
Published 5 February 2019

**Abstract**

Gyrokinetic simulations of DIII-D tokamak with axisymmetric equilibrium show that the reduction in the radial electric field shear at the top of the pedestal during edge localized mode (ELM) suppression with the $n = 2$ resonant magnetic perturbations (RMPs) leads to enhanced drift-wave turbulence and extended turbulence spreading to the top of the pedestal relative to ELMing plasmas with similar RMP and pedestal parameters. The simulated turbulent transport at the top of the pedestal in ELM suppressed conditions is consistent with experimental observations of enhanced turbulence at the top of the pedestal during ELM suppression by the RMPs. These results imply that enhanced drift-wave turbulence due to reduced $E \times B$ shear at the pedestal top can contribute to the additional transport required to prevent the pedestal growing to a width that is unstable to ELMs.

Keywords: RMP turbulence, $E \times B$ shear, edge localized modes, resonant magnetic pertubations, DIII-D, gyrokinetic simulations, plasma

(Some figures may appear in colour only in the online journal)

## 1. Introduction

In order to achieve the required confinement for producing significant fusion gain, the high confinement mode (H-mode) is the selected mode of operation in the International Thermonuclear Experimental Reactor (ITER). However, along with the H-mode come edge localized modes (ELMs), or intermittent magnetohydrodynamic (MHD) bursts, that can produce substantial pulses of thermal energy from the plasma edge to the plasma facing components. While ELMs are benign in present day experiments, extrapolations to reactor scale (such as ITER) predict ELM energy fluxes of up to 20 MJ in fractions of a millisecond [1], which can drastically decrease divertor lifetimes, generate impurities, and erode first wall components. Resonant magnetic perturbations (RMPs) have been shown to mitigate and/or suppress ELMs in DIII-D [2–4] and in many other fusion experiments [5–8]. A leading hypothesis is that ELM stabilization by RMPs is achieved by significantly increasing the edge plasma transport, preventing the pedestal from reaching the Peeling–Ballooning-Mode (PBM) stability boundary [4, 9].

The observation of spontaneous transitions between ELMing and ELM suppressed conditions with static $n = 2$ RMPs reveals that ELM suppression is achieved or lost via a bifurcation in magnetic fields near the inner wall, pedestal impurity toroidal rotation velocity and density fluctuations [10]. Another study using modulated $n = 3$ RMPs in an ELM suppressed state revealed a prompt increase in ion-scale density fluctuations with the increase in the RMP level, indicative of a direct effect of the RMP on turbulence at the pedestal top [3]. Still other studies have revealed increased density fluctuations at intermediate scales at the pedestal top in the transition to ELM suppression [11, 12]. These observations suggest that enhanced top of pedestal turbulent fluctuations may play some role in the suppression of ELMs, consistent with an earlier hypothesis that enhanced top of pedestal transport is required to suppress ELMs [9].

The effect of the RMP on edge transport changes observed during ELM suppression likely involves a number of factors associated with the resonant and nonresonant effects of the RMP on the plasma. Nonresonant effects are associated with the plasma kink response to the external field and do not involve a topology change in the plasma. Resonant effects involve a change in topology resulting from magnetic island formation and possible magnetic stochasticity when the islands overlap [10]. How these resonant and nonresonant effects influence transport to suppress ELMs has been the subject of extensive research.

From first principles global gyrokinetic simulations, using the gyrokinetic toroidal code (GTC) [13, 14], it has been demonstrated that the effect of the ideal MHD component of the plasma (kink) response to the RMP has a negligible effect on the linear growth rate of microturbulence and zonal flows at the top of the pedestal, in DIII-D ITER similar shape plasmas for experimentally relevant values of the RMP, ($\delta B/B \approx 5 \times 10^{-4}$) [15]. This work suggests that the main nonresonant effect of the RMP on transport is through the neoclassical ambipolar potential or the neoclassical toroidal viscosity (NTV) [16], which can result in changes to the radial electric field ($E_r$) and its shear.

The effect of magnetic stochasticity on edge transport due to magnetic island overlap has also been explored. However, it is clear from detailed profile measurements on DIII-D that the presence of stochasticity is incommensurate with the inferred electron thermal transport at the top of the pedestal [17]. Therefore, any magnetic resonant mechanism that purports to account for enhanced thermal transport at the top of the pedestal must be a property of isolated non-overlapping magnetic islands. Regardless of the dominant mechanism behind the change in the radial electric field, we need to explore how this change can affect thermal and particle transport in the case where there are good (confining) magnetic surfaces between isolated (small) magnetic islands.

In this paper, we show that there is a plausible mechanism to account for the increase in ion-scale turbulence and transport at the top of the pedestal during RMP induced ELM suppression, resulting from the modification of the $E_r$ profile due to $n = 2$ RMPs in the DIII-D tokamak. The mechanism involves a flattening of the $E_r$ profile at the pedestal top, thereby significantly reducing the local $E \times B$ shearing rate. Indeed, figure 3(*c*) in [10] shows a strong flattening of the $E_r$ profile (and hence reduction of the $E \times B$ shear) at the pedestal top ($\rho \approx 0.92$) in the transition to ELM suppression. However, we cannot claim that the reduction of $E \times B$ shear is the cause of the turbulence increase in all cases of RMP ELM suppression. A recent study of ELM suppression with $n = 3$ RMP reveals no significant increase in the top of pedestal ion scale fluctuations, nor a significant decrease in the $E \times B$ shear in the transition to ELM suppression (see figure 13 in [12]). Another study using modulated $n = 3$ RMPs in an ELM suppressed state indicated that an increase in ion-scale turbulence with increasing RMP level before an observable change in the $E \times B$ shear [3]. We also note that an increase in fluctuations at intermediate scales ($k\rho_s > 2$) is seen during $n = 2$ and $n = 3$ ELM suppression [11, 12]. These various studies performed under different plasma conditions and with different RMP fields yield a somewhat confusing array of results. These results indicate that a comprehensive assessment of the conditions in ELM suppression over a wide range of conditions is needed.

A comprehensive assessment of prompt fluctuation and $E \times B$ shear changes in the transition to ELM suppression is beyond the scope of this paper. Therefore, we only confine our present study to the analysis of $n = 2$ RMP ELM suppressed plasmas in the ITER similar shape on DIII-D with static $n = 2$ RMPs, where a concomitant reduction in the $E \times B$ shear is seen with the increase in the turbulent fluctuations at the pedestal top in the transition to ELM suppression.

It is well known that the reduction of $E \times B$ shear can have a direct effect on driftwave turbulence and transport [18]. Using GTC simulations, we show that the reduction of the $E \times B$ shear near the pedestal top has a direct effect, in axisymmetric geometry, on driftwave turbulence and transport in DIII-D shot 158103 with $n = 2$ RMPs [10]. Specifically, our simulations find that the weaker $E \times B$ shearing rate in the ELM suppressed state allows ITG-like turbulence in the DIII-D plasma outer edge to nonlinearly spread [19] to the pedestal top. This spreading leads to a broader region of microturbulence and larger calculated turbulent transport at the pedestal top. The increase in driftwave turbulence is not present in two corresponding ELMing cases, namely, shots 158103 at 3750 ms (ELMing with the same $n = 2$ RMP) and 158104 at 1350 ms (ELMing without RMP). All simulations reported in this paper are electrostatic, since the kinetic ballooning mode was found to be marginally stable in the DIII-D pedestal top, while electrostatic ion temperature gradient (ITG) types of instabilities are strongly unstable [20–22]. Our result demonstrates a plausible mechanism for the observed increase in pedestal top turbulence and transport, driven by $n = 2$ RMPs through reduced $E \times B$ shear. However, we note that this work does not address the mechanism by which the RMP modifies the $E \times B$ shear. This goal of this study is to examine the effects of changes in axisymmetric profiles on turbulence and transport in the DIII-D tokamak pedestal top, for $n = 2$ RMP experiments in ITER-like plasmas.

The rest of this paper is structured as follows. In section 2, we extend the fluid kinetic electron hybrid model [23] to simulate the electron response with an equilibrium radial electric field. The new model is verified, in simple geometry, in section 3. In section 4, we apply our model on three DIII-D test cases, two of which are ELMing, one with and the other without $n = 2$ RMP and the third is an $n = 2$ RMP ELM suppressed case. We find that the reduced equilibrium $E \times B$ shearing rate in the $n = 2$ RMP ELM suppressed case leads to enhanced microturbulence and transport at the pedestal top, consistent with experimental observations of increased ion-scale fluctuations at the pedestal top [10].

## 2. Simulation model

In GTC, ions (and electrons) are simulated [24] by integrating the gyrokinetic (driftkinetic) equation along gyrocenter trajectories, and the effects of an equilibrium radial electric field enter via the equations of motion. However, electrons are simulated in this work via the fluid-kinetic hybrid model [23], for which an extension to incorporate an equilibrium radial electric field is presented here. No modification to the ion model is needed, as ions use the $\delta f$ method [25], which evolves the perturbed ion distribution by integrating the perturbed part of the gyrokinetic equation operator operating on the equilibrium ion distribution.

### 2.1. Gyrokinetic equations in toroidal geometry

In the electrostatic and collisionless limit, the gyrokinetic equation [25, 26] for toroidal plasmas in five dimensional phase space with gyrocenter position $\mathbf{X}$, magnetic moment $\mu$, and parallel velocity $v_\parallel$ is,

$$L f_\alpha(\mathbf{X},\mu,v_\parallel,t) \equiv \left[\frac{\partial}{\partial t} + (v_\parallel \mathbf{b}_0 + \mathbf{v}_d + \mathbf{v}_E)\cdot\nabla - \mathbf{b}_0^* \cdot (\mu\nabla B_0 + Z_\alpha \nabla\phi)\frac{\partial}{m_\alpha \partial v_\parallel}\right] f_\alpha = 0, \tag{1}$$

where,

$$\begin{aligned}
\mathbf{v}_E &= \frac{c\mathbf{b}_0\times\nabla\phi}{B_0},\\
\mathbf{v}_d &= \frac{\mu}{m_\alpha\Omega_\alpha}\mathbf{b}_0\times\nabla B_0 + \frac{v_\parallel^2}{\Omega_\alpha}\nabla\times\mathbf{b}_0,\\
\mathbf{b}_0^* &= \mathbf{b}_0 + \frac{v_\parallel}{\Omega_\alpha}\nabla\times\mathbf{b}_0,\\
\Omega_\alpha &= \frac{Z_\alpha B_0}{m_\alpha c}.
\end{aligned} \tag{2}$$

$\alpha$ represents the particle species, and $m_\alpha$, $Z_\alpha$, and $\mathbf{B}_0 = B_0\mathbf{b}_0$ are the particle mass, particle charge, and equilibrium magnetic field, respectively. Also, the perturbed gyroaveraged electrostatic potential, $\phi = \delta\phi + \phi_{ZF}$, is separated into nonzonal and zonal components. Now, the operator $L$ can be separated into equilibrium, nonzonal, and zonal parts. Specifically,

$$L = L_0 + \delta L + L_{ZF} \tag{3}$$

where,

$$\begin{aligned}
L_0 &= \frac{\partial}{\partial t} + (v_\parallel\mathbf{b}_0 + \mathbf{v}_d)\cdot\nabla - \mathbf{b}^*\cdot\mu\nabla B_0\frac{\partial}{m_e\partial v_\parallel},\\
\delta L &= \delta\mathbf{v}_E\cdot\nabla - \mathbf{b}^*\cdot Z_e\nabla\delta\phi\frac{\partial}{m_e\partial v_\parallel},\\
L_{ZF} &= \frac{c\mathbf{b}_0\times\nabla\phi_{ZF}}{B_0}\cdot\nabla - \frac{v_\parallel}{\Omega_\alpha}\nabla\times\mathbf{b}_0\cdot Z_\alpha\nabla\phi_{ZF}\frac{\partial}{m_\alpha\partial v_\parallel},
\end{aligned} \tag{4}$$

and, $\delta\mathbf{v}_E = \frac{c\mathbf{b}_0\times\nabla\delta\phi}{B_0}$.

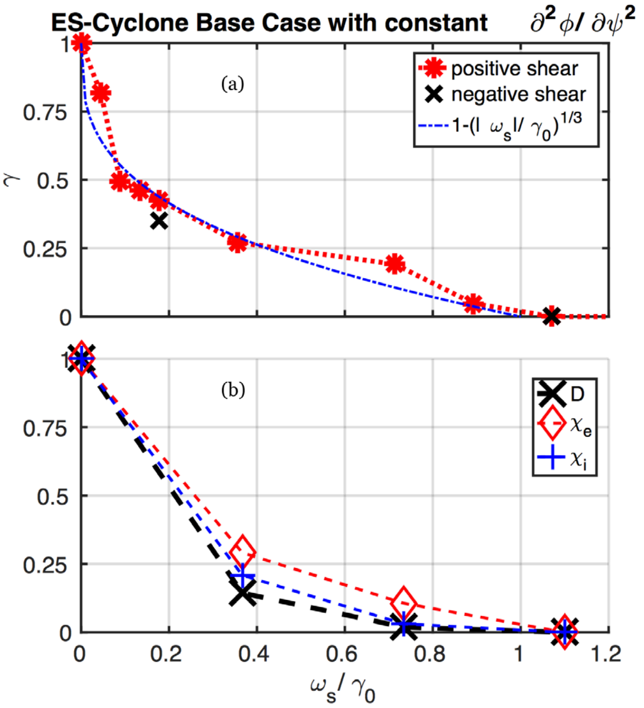

**Figure 1.** Simulations results of the cyclone base case with constant $\partial^2\phi/\partial\psi^2$. (*a*) The growth rate and (*b*) the heat and particle diffusivity transport coefficients versus $\omega_s$ normalized to $\gamma_0$, the growth rate when $\omega_s = 0$. All plotted quantities are normalized to their respective values when $\omega_s = 0$.

### 2.2. Electron kinetic response

The electron response is separated into equilibrium and perturbed parts, $f_e = f_{e0} + \delta f_e$, with,

$$L_0 f_{e0} = 0, \tag{5}$$

defining the equilibrium distribution, the neoclassical solution. After substituting for $f_e$, we can rewrite equation (1) as,

$$\begin{aligned}
L\delta f_e &= -L f_{e0}\\
&= -(\delta L + L_{ZF}) f_{e0},
\end{aligned} \tag{6}$$

where, for simplicity, we approximate the source with a local Maxwellian, i.e. $f_{e0} \approx \frac{n_{e0}}{(2\pi T_e/m_e)^{3/2}}\exp[-(2\mu B_0 + m_e v_\parallel^2)/2T_e]$.

The fluid-kinetic hybrid model will further take the perturbed part of the distribution and split it into a larger adiabatic part, $\delta f_e^{(0)}$, and a smaller non-adiabatic part, $\delta h_e$. Namely, $\delta f_e = \delta f_e^{(0)} + \delta h_e$, with $|\delta f_e^{(0)}| >> |\delta h_e|$. This latter separation saves immensely on computational costs by analytically removing high frequency modes (the so-called $\omega_H$ mode [27]), which reduces particle noise associated with the adiabatic electrons. To obtain an expression for $\delta f_e^{(0)}$, we expand equation (1) to first order in $\omega/k_\parallel v_\parallel$:

$$\begin{aligned}
v_\parallel\mathbf{b}_0\cdot\nabla\delta f_e^{(0)} - \mathbf{b}_0\cdot Z_e\nabla\delta\phi\frac{\partial}{m_e\partial v_\parallel}f_{e0} &= 0,\\
\delta f_e^{(0)} &= -\frac{Z_e\delta\phi}{T_e}f_{e0}.
\end{aligned} \tag{7}$$

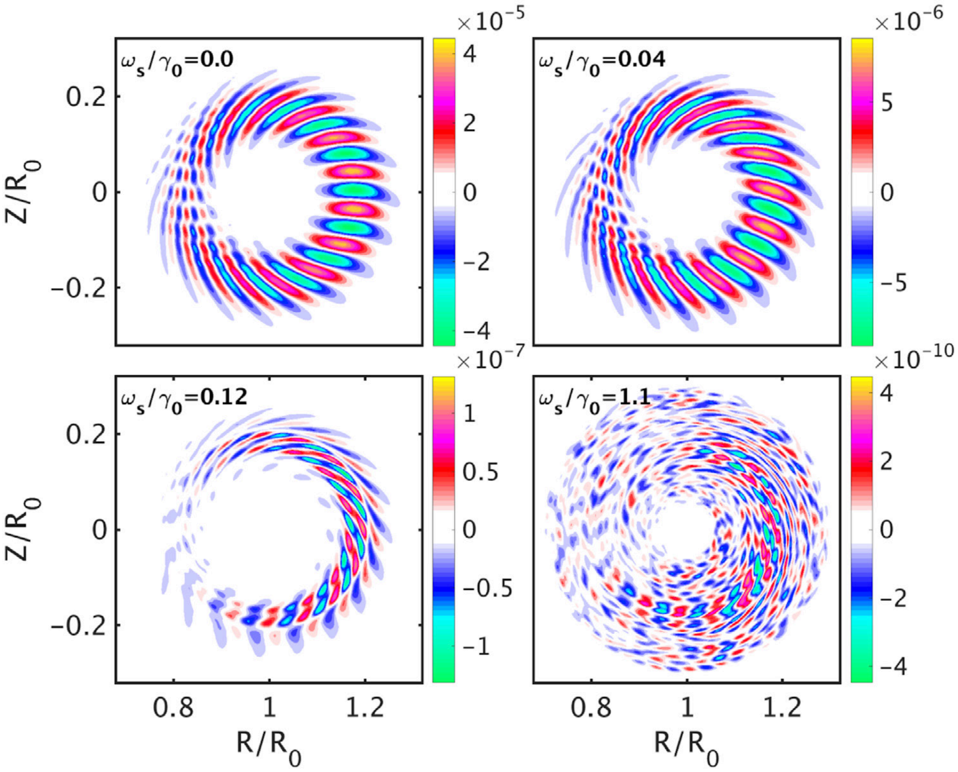

**Figure 2.** 2D linear mode structures, of the perturbed electrostatic potential, for four points of figure 1(*a*). Each snapshot is taken at the same physical time and each simulation uses the same initialization.

Equation (6) can now be rewitten as,

$$L\delta h_e = -L(f_{e0}+\delta f_e^{(0)}) = -(\delta L + L_{ZF})f_{e0} - f_{e0}(L_0+L_{ZF})\frac{\delta f_e^{(0)}}{f_{e0}}. \tag{8}$$

After simplifying, equation (8) becomes,

$$L\delta h_e = f_{e0}\left[\frac{\partial}{\partial t}\frac{Z_e\delta\phi}{T_e} - \delta\mathbf{v}_E\cdot\nabla\ln f_{e0}|_{v_\perp,v_\parallel} - (\mathbf{v}_d+\delta\mathbf{v}_E)\cdot\nabla\left(\frac{Z_e\phi_{ZF}}{T_e}\right)\right]. \tag{9}$$

### 2.3. Equilibrium radial electric field

To add the effects of the radial electric field, the definition of the electrostatic potential is extended to include an equilibrium part:

$$\phi = \delta\phi + \phi_{ZF} + \phi_{\rm eq}, \tag{10}$$

where, $\phi_{\rm eq}$ is the equilibrium potential. $L_0$ now becomes,

$$L_0 = \frac{\partial}{\partial t} + (v_\parallel\mathbf{b}_0 + \mathbf{v}_d + \mathbf{v}_{E_{\rm eq}})\cdot\nabla - \mathbf{b}^*\cdot\mu\nabla B_0\frac{\partial}{m_e\partial v_\parallel}, \tag{11}$$

where, the new term in the operator is $\mathbf{v}_{E_{\rm eq}} = \frac{c\mathbf{b}_0\times\nabla\phi_{\rm eq}}{B_0}$. This additional term, associated with the equilibrium radial electric field in equations (10) and (11), as well as the nonlinear propagator $L$, is now added to the ion gyrokinetic equations in section 2.1. Regarding electron drift kinetic equation, equation (9) now becomes,

$$L\delta h_e = f_{e0}\left[\frac{\partial}{\partial t}\frac{Z_e\delta\phi}{T_e} - \delta\mathbf{v}_E\cdot\nabla\ln f_{e0}|_{v_\perp} + \mathbf{v}_{E_{\rm eq}}\cdot\nabla\frac{Z_e\delta\phi}{T_e} - (\mathbf{v}_d+\delta\mathbf{v}_E)\cdot\nabla\left(\frac{Z_e\phi_{ZF}}{T_e}\right)\right]. \tag{12}$$

Assuming $k_\perp L_T \gg 1$, the new term in equation (12) can be combined with the second term yielding,

$$L\delta h_e = f_{e0}\left[\frac{\partial}{\partial t}\frac{Z_e\delta\phi}{T_e} - \delta\mathbf{v}_E\cdot\nabla\left(\ln f_{e0}|_{v_\perp,v_\parallel} + \frac{Z_e\phi_{\rm eq}}{T_e}\right) - (\mathbf{v}_d+\delta\mathbf{v}_E)\cdot\nabla\left(\frac{Z_e\phi_{ZF}}{T_e}\right)\right]. \tag{13}$$

With the equilibrium radial electric field, there is the associated equilibrium toroidal flow needed to satisfy equation (5). This necessitates the approximated equilibrium particle distribution becoming a shifted maxwellian: $f_{e0} \approx \frac{n_{e0}}{(2\pi T_e/m_e)^{3/2}}\exp[-(2\mu B_0 + m_e(v_\parallel - v_{\parallel 0})^2/2T_e)]$, where $v_{\parallel 0} \approx R\Omega_\phi$ is the equilibrium parallel velocity, with equilibrium toroidal rotation $\Omega_\phi$ and major radius $R$. The toroidal rotation can be calculated from radial force balance, $\Omega_\phi = -\partial\phi_{\rm eq}/\partial\psi - \frac{1}{n_i Z_i}\partial P_i/\partial\psi + q\Omega_\theta$, where $n_i$ and $P_i$ are the ion density and pressure, $q$ and $\Omega_\theta$ are the magnetic

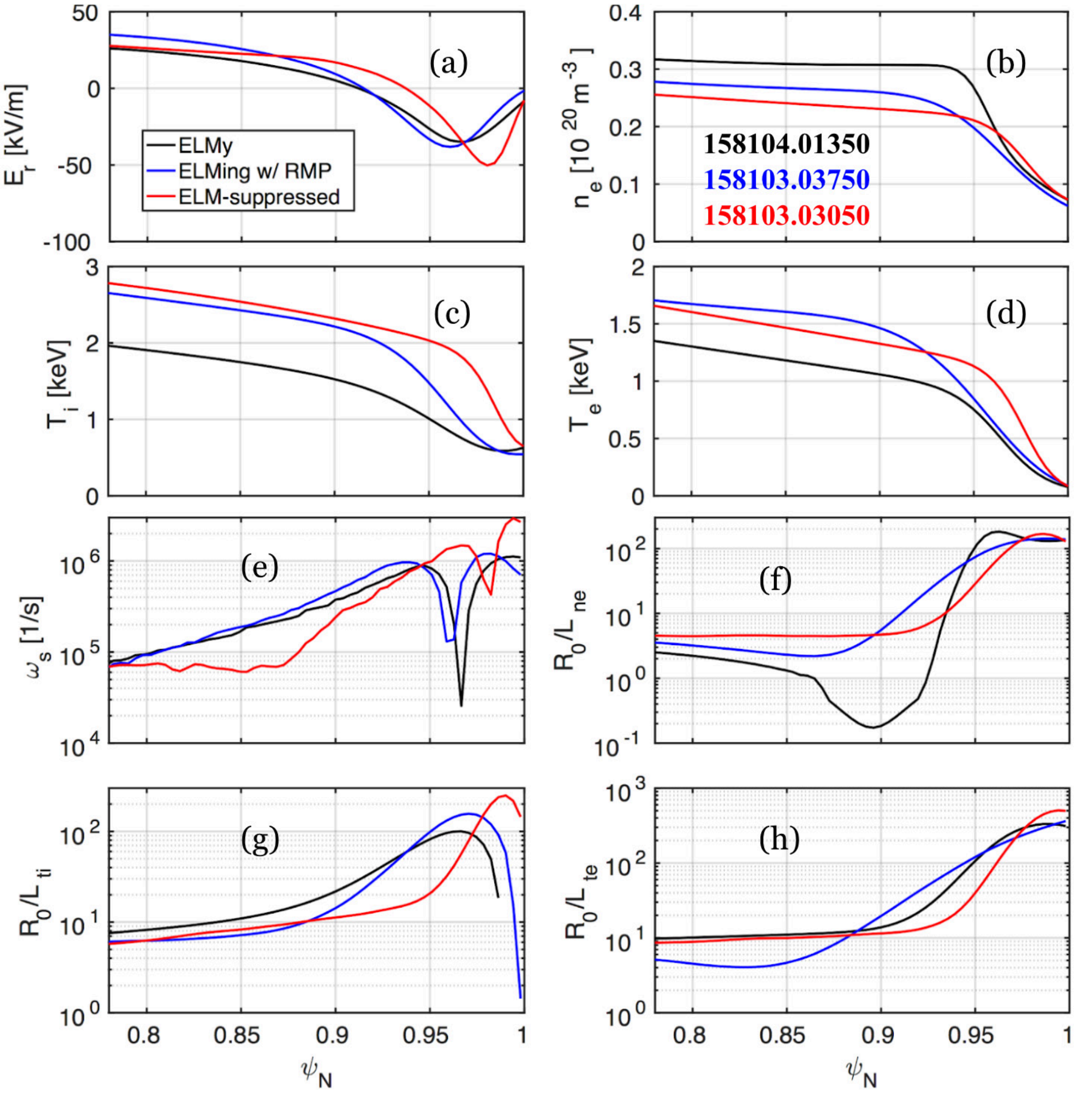

**Figure 3.** Equilibrium plasma profiles from DIII-D shot 158104 @ 01350 ms (ELMing case before RMP, black), 158103 @ 03750 ms (ELMing with RMP, blue), and 158103 @ 03050 ms (RMP ELM suppressed, red) [10]. (*a*) Equilibrium radial electric field. (*b*) Electron density. (*c*) Ion temperature. (*d*) Electron temperature. (*e*) $E_r$ shearing rate, $\omega_s$. (*f*) Electron density scale length. (*g*) Ion temperature scale length. (*h*) Electron temperature scale length. The pedestal top region corresponds to $\psi_n = [0.9, 0.95]$.

safety factory and poloidal rotation, and $\psi$ is the poloidal flux. However, for computational efficiency we ignore the effects of the equilibrium flows, $v_{\parallel 0}$, for ions and electrons, as our simulations find that their effects are small for the experimental values of $v_{\parallel 0}$.

## 3. Verification of radial electric field shear effects

To verify the formulation and implementation of radial electric field shear effects, a set of benchmarks are prepared using simple toroidal geometry with profiles and parameters being taken from the well known Cyclone base case [28]. Specifically, the cyclone base case consists of an electrostatic system, an axisymmetric tokamak with circular cross sections, a hydrogenic plasma, a magnetic safety factor, $q = 0.8\psi_N + 1.1\psi_N + 1.0\psi_N^2$, where $\psi_N$ is the poloidal magnetic flux normalized to the separatrix value, $T_i = T_e$, $R_0/L_{T_i} = R_0/L_{T_e} = 6.9$, $R_0/L_n = 2.2$, $a/R_0 = 0.36$, where $L_x = \frac{\partial \log x}{\partial r}$ is the scale length of quantity $x$, $R_0$ is the major radius at the magnetic axis, $a$ is the minor radius at the plasma edge, and $r = 0.5a$. With these parameters, the system contains an unstable ITG mode, with the single toroidal mode number $n = 10$. Also, these parameters yield $k_\theta \rho_i = 0.22$, which is the dominant wavenumber observed in nonlinear simulations of this case. ITG simulations with these parameters have previously been studies in [29].

Firstly, the effects of rigid rotation, $\partial\phi_{\mathrm{eq}}/\partial\psi_N = \mathrm{const.}$, are tested, where the Mach number due to the $E_r$ induced parallel flow, $M = v_{\parallel 0}/C_s$, with $C_s = \sqrt{T_e/m_i}$ being the sound speed, is scanned in the range $M = [0, 0.25]$. The expectation is that for $M \ll 1$ the effects of rigid rotation should be negligible. GTC find that for the case of largest Mach number, $M = 0.25$, the ITG growth rate is found to vary by 1%, within the error of the measurement. For context, value of $M$ in the pedestal top region of DIII-D, for the cases to be examined in this work, is about 0.20. Moreover, if the newly added term

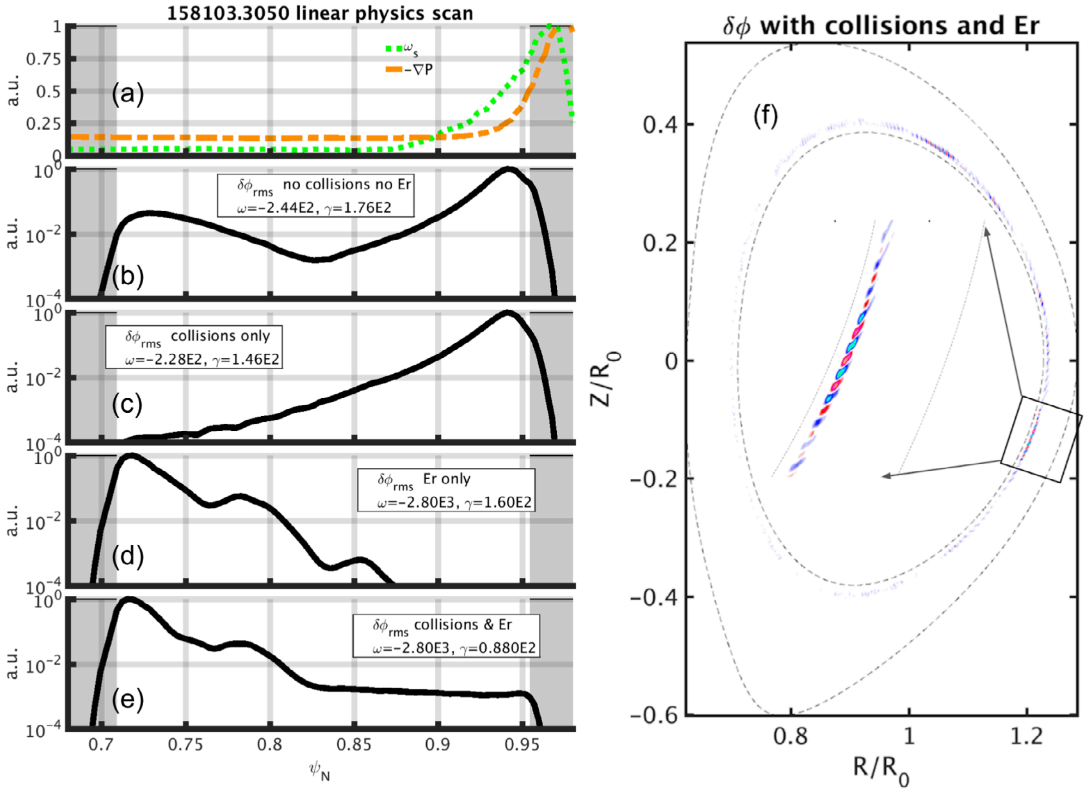

**Figure 4.** GTC linear electrostatic simulations, with various physics included, of the RMP induced ELM suppressed case, DIII-D shot 158103 at 03050 ms. (*a*) The equilibrium pressure gradient and $E \times B$ shearing rate. ((*b*)–(*e*)) Radial mode structure of the perturbed electrostatic potential with various physics are plotted. Observed rates (in the lab frame) are given in the legend. Real frequencies and growth rates are in units of kHz and krad/s, respectively. Mode amplitudes are normalized in each panel according to each panel's respective maximum value. (*f*) The perturbed electrostatic potential, for the collisions and $E_r$ case, in a poloidal cross section.

in equation (13) is omitted from the simulation and $E_r$ effects only enter the system via the equations of motion, a large electron response to the uniform radial electric field is observed. This signifies that the new term in the electron $\delta h$ equation is very important in capturing the physics under consideration.

Secondly, the effects of $E_r$ shear, $\omega_s = \frac{(RB_p)^2}{B}|\partial^2\phi_{\mathrm{eq}}/\partial\psi^2|$, are considered. In this case, all simulation parameters are the same as above, except $\omega_s$ is scanned in the range $\omega_s/\gamma_0 = [0, 1.1]$, where $\gamma_0$ is the maximum linear growth rate in the absence of $E_r$ shear, and $\partial\phi_{\mathrm{eq}}/\partial\psi = 0$ in the middle of the simulation domain. Figure 1(*a*) shows the simulated ITG growth rate versus the magnitude of $\omega_s$, which are both normalized to $\gamma_0$. As the magnitude of the shear is increased, the instability growth rate decreases, roughly as $|\omega_s|^{1/3}$, until it completely goes to zero near $\omega_s/\gamma_0 = 1$. Also, the stabilization of $E_r$ shear does not depend on the sign of the shear. Moreover, when $\omega_s$ roughly equals the maximum growth rate, the ITG mode is completely stabilized. This is depicted in figure 2, where the 2D mode structures, of the perturbed electric potential, for four points, corresponding to $\omega_s/\gamma_0 = 0.0, 0.04, 0.12, 1.1$, from figure 1(*a*) are shown. All four mode structures are taken from the same physical time in each simulation and use the same initial conditions. Thus, the magnitudes from each figure can be compared to one another.

The $\omega_s$ scaling is further extended to nonlinear simulations of the Cyclone base case, to study the effect of $\omega_s$ on transport and zonal flows. Figure 1(*b*) shows the heat conductivity and particle diffusivity, versus $\omega_s/\gamma_0$. All plotted quantities are normalized to their respective values when $\omega_s = 0$. As expected, all quantities display a similar behavior as the ITG growth rate in figure 1(*a*), as they are seen to vanish as $\omega_s/\gamma_0$ approaches unity.

## 4. Simulations of microturbulence in DIII-D pedestal top

Here we use as input to GTC the equilibrium profiles obtained from $n = 2$ ELM suppression studies reported in [10]. In [10], a concomitant flattening of the $E \times B$ shear and increase in ion-scale fluctuations is seen at the top of the pedestal in the ELM suppressed state compared to ELMing conditions with the same level of RMP. Similarly, a reduction in turbulence and transport is seen in the transition from ELM suppression to ELMing conditions. The reduction in the fluctuations is correlated with an increase in the top of pedestal $E \times B$ shear. Here we analyze three kinetic equilibria generated from the data collected in the $n = 2$ RMP experiment. The first, for discharge #158104 is taken at $t \approx 1350$ ms during the ELMing phase before the $n = 2$ RMP is turned on. The second and third equilibria are from discharge #158103 during $n = 2$ RMP ELM suppression at $t \approx 3050$ ms and during ELMing conditions with RMP at $t \approx 3750$ ms, respectively. A description of

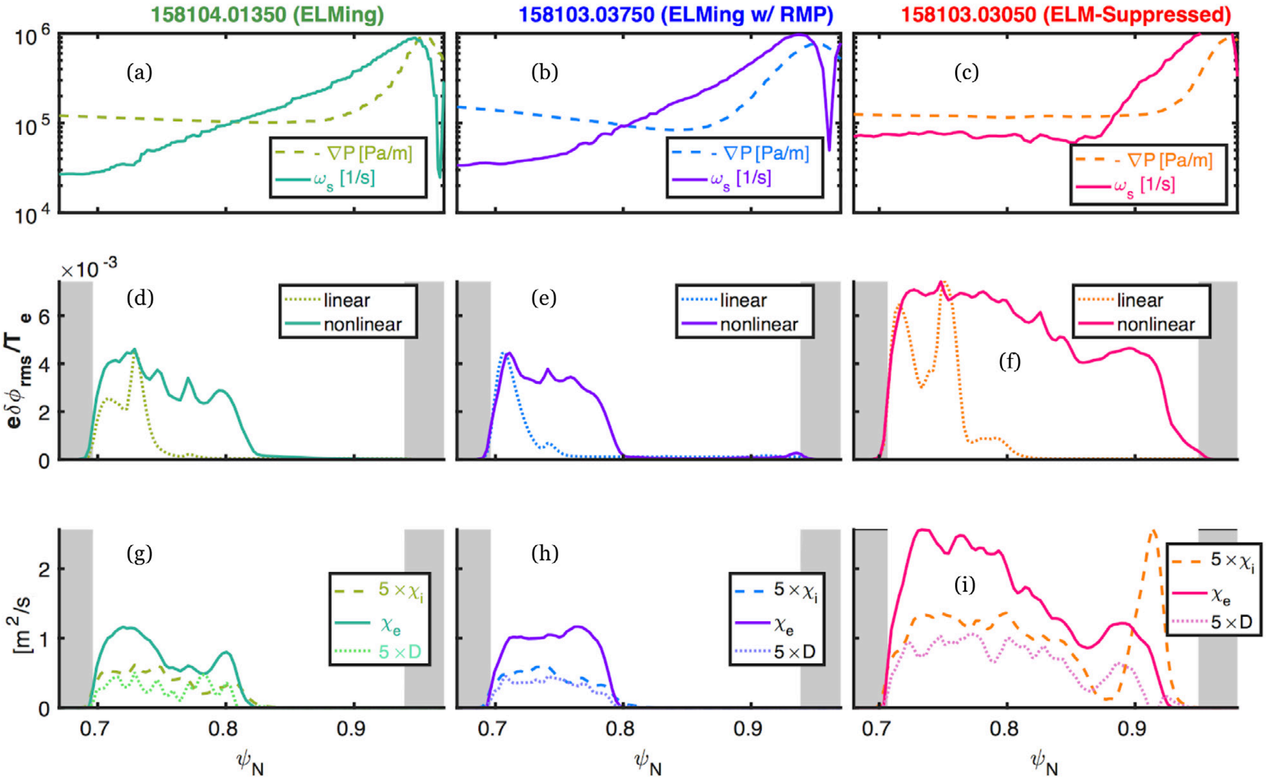

**Figure 5.** GTC simulation inputs and results from three nonlinear simulations: DIII-D shots 158104.01350 (ELMing, first column), 158103.03750 (ELMing with RMP, second column), and 158103.03050 (ELM-suppressed via RMPs, third column). All physical units are in SI units where applicable. ((*a*)–(*c*)) Pressure drive and Er shear rate radial profiles. ((*d*)–(*f*)) flux-surface-rms-averaged potential profiles for both linear and nonlinear phases. ((*g*)–(*i*)) Transport coefficients: ion and electron heat conductivities, and particle diffusivity.

the plasma conditions can be found in [10] and a description of the $n = 2$ RMP field amplitude and spectrum can be found in [30].

Figure 3 shows the profiles for these three sets of DIII-D equilibria. By comparing the scale length profiles, we see that the ELM suppressed case has lower $R_0/L_n$ and $R_0/L_T$ at the pedestal top ($\psi_n \approx 0.94$), when compared to the ELMing cases. In the absence of $E \times B$ shear, these profile changes will tend to reduce the drive for ion scale turbulence in ELM suppression, relative to ELMing conditions. However, using GTC simulations, we show that the reduction in the $E \times B$ shear during ELM suppression (shown in figure 3(*e*)) leads to an overall increase in the top of pedestal ion scale turbulence, consistent with experiment.

### 4.1. Simulation setup

In the following simulations, numerical convergence has been obtained. The number of particles per cell, for both ions and electrons, is 100 or 10 for nonlinear or linear simulations, respectively. The time step used is $\Delta t C_s/R_0 = 0.008$. The spatial resolution is $\Delta r/\rho_i \sim r\Delta\theta/\rho_i \sim 0.25$, and there are 32 poloidal cross-sections in the whole torus. The radial domains used are $\psi_N = [0.67, 0.97]$ for 158104.01350 and 158103.03750, and $\psi_N = [0.68, 0.98]$ for 158103.03050, where $\psi_N$ is the normalized poloidal flux. The perturbed electric field is solved with a Dirichlet boundary condition, and neither toroidal nor poloidal filtering is performed on the solution. Profiles are measured using active carbon charge exchange spectroscopy and Thomson scattering measurements, as described in [10], and 3D magnetic equilibria are obtained from VMEC [31]. Since the effects of 3D magnetic perturbation with closed flux surface on the pedestal top turbulence [15] was found to be small in earlier GTC simulations, only the axisymmetric $n = 0$ equilibrium profiles are kept in this work, so as to focus our study on the effects of the profile differences between ELMing and ELM suppressed plasmas. When using collisions we use the electron-ion Lorentz scattering model and in this case $\nu_{e,i} \approx \nu_{e,e} \gg \nu_{i,i}$, with $\nu^* = \nu_{e,i}/\omega_{b,e} = 0.031$, where $\omega_{b,e}$ is the electron bounce frequency.

### 4.2. Effects of $E_r$ shear and collisions on linear instabilities

Linear GTC simulation results for the ELM suppressed case (#158103 at 3050 ms) show the effects of $E_r$ and collisions on the linear growth rates. Figures 4(*b*)–(*e*) illustrates the linear radial mode structures of the perturbed electrostatic potentials from four different linear GTC runs. Each simulation contains different physics: no collisions and no $E_r$ (base case), collisions only, $E_r$ only, and collisions and $E_r$ (comprehensive case). For reference, the equilibrium pressure gradient (orange) and $E \times B$ shearing rate ($\omega_s$, green) profiles are also depicted in figure 4(*a*). In all four cases the unstable modes

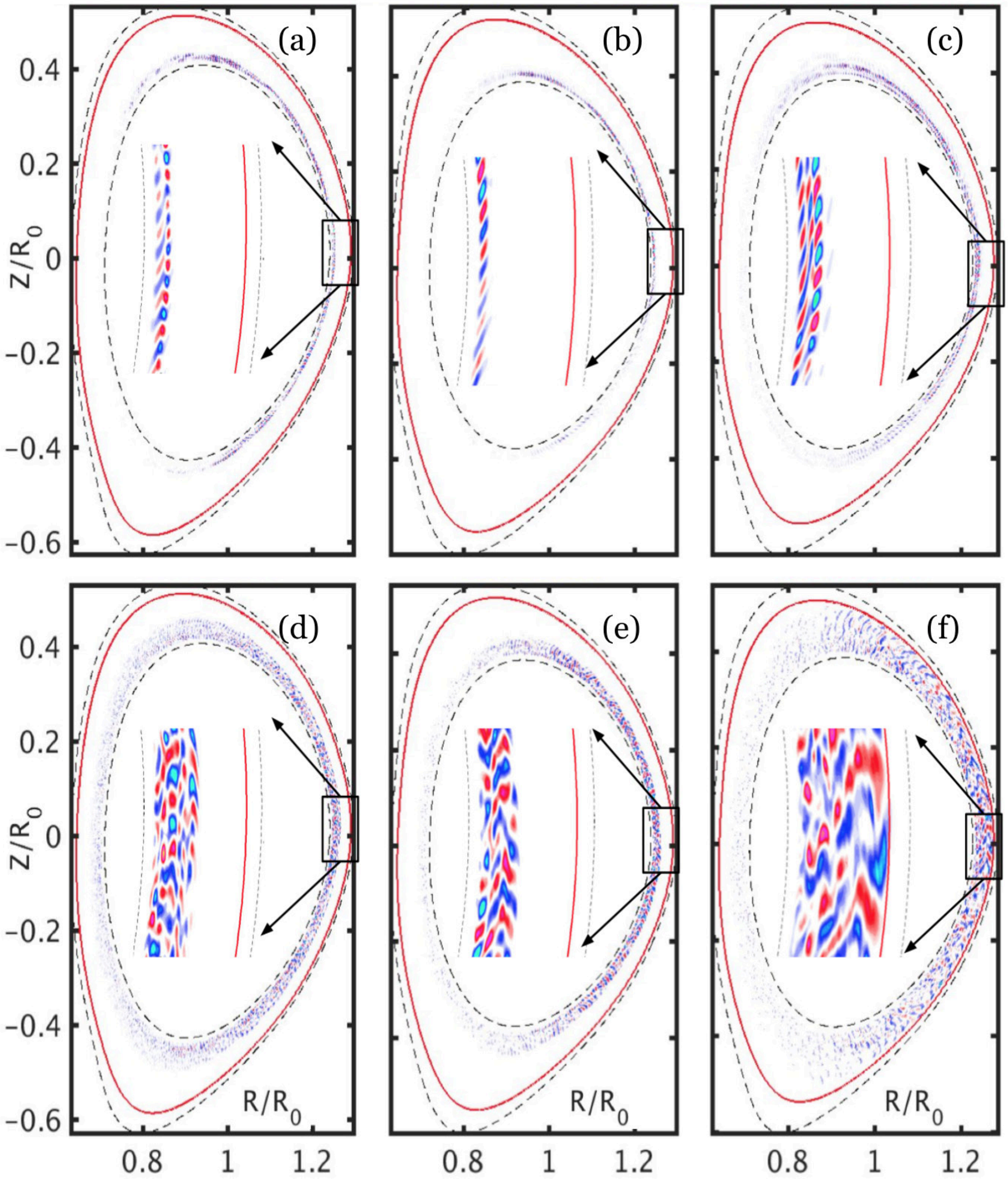

**Figure 6.** 2D poloidal cross sections of linear ((*a*)–(*c*)) and nonlinear ((*d*)–(*f*)) phases of electrostatic fluctuations from GTC simulations of DIII-D shots 158104.01350 (ELMing, first column), 158103.03750 (ELMing with RMP, second column), and 158103.03050 (ELM-suppressed via RMPs, third column). The black dashed lines trace out the simulation boundaries, and the red solid lines mark the location of the $q = 4$ surface in each case.

were found to be ITG-like, as they are strongly enhanced by kinetic electrons [23] and rotate in the ion diamagnetic direction. The dominant modes are found to have $k_\theta \rho_i \approx 1$, however nonlinear simulations to be shown in section 4.3 will show that smaller wavenumbers are also present yet with smaller growth rates. Due to the steep gradients in the simulation domain, the growth rate is close to linear frequency, the mode is not conventional ITG even though the frequency is still in the ion direction [20–22]. It is more like electrostatic interchange mode [20–22]. We note that the the inclusion of kinetic electrons is necessary for accurate modeling of the experimental case under consideration, as the trapped electron enhancement of the ITG-like instabilities is observed to be significant.

The base case without collisions or $E_r$ (figure 4(*b*)) shows the modes dominantly localized in the top of pedestal region, $\psi_n > 0.93$, with some activity near $\psi_n = 0.73$. Adding collisions (figure 4(*c*)) decreases the real frequency and growth rate by 5% and 17%, respectively, and the fluctuations near $\psi_N = 0.73$ are no longer seen. For $E_r$ only with no collisions (figure 4(*d*)) the growth rate decreases by 9% and the real frequency increases substantially in the lab frame, due to the

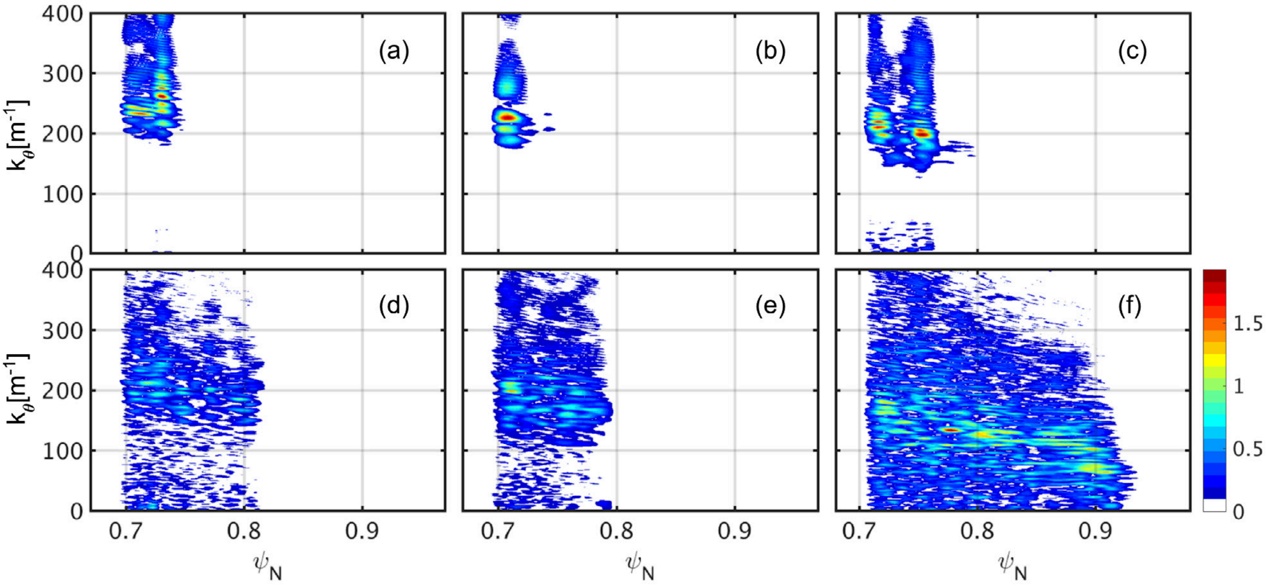

**Figure 7.** Poloidal wavenumbers of fluctuation spectra of linear ((*a*)–(*c*)) and nonlinear ((*d*)–(*f*)) phases of electrostatic fluctuations from GTC simulations of DIII-D shots 158104.01350 (ELMing, first column), 158103.03750 (ELMing with RMP, second column), and 158103.03050 (ELM-suppressed via RMPs, third column). Nonlinear magnitudes are given on the same scale for comparison, while linear magnitudes are arbitrary and simply indicate the dominant radial and spectral locations.

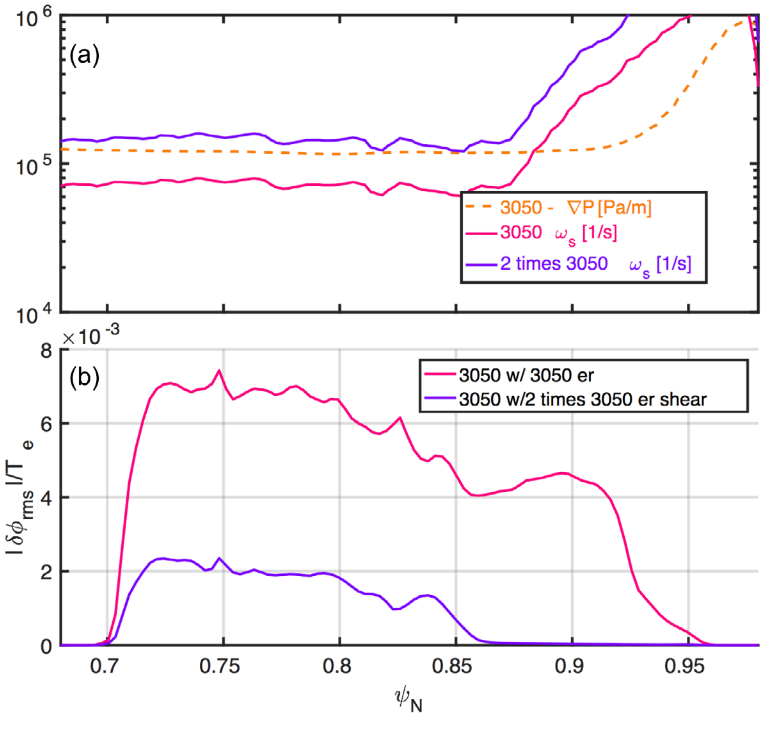

**Figure 8.** GTC simulation inputs and results from two nonlinear simulations: DIII-D shot 158103.03050 (ELM-suppressed via RMPs) with its original $E \times B$ shear profile and with its $E \times B$ shear profile scaled up by a factor of two. (*a*) Pressure drive and Er shear rate radial profiles. (*b*) flux-surface-averaged potential profiles for the nonlinear phase of the original $E \times B$ shear (red) and two times increased $E \times B$ shear (purple) cases.

$E_r$ induced Doppler shift. The large $E_r$ shear in the pedestal stabilizes the interchange modes beyond $\psi_n > 0.83$, leaving unstable modes confined to $\psi_n < 0.83$, with peak amplitude at $\psi_n \approx 0.72$. Lastly, the mode structure for the comprehensive case (figure 4(*e*)) is similar to the case with $E_r$ only, however, the growth rate is lower by 50% due to collisions. The reduction of the growth rate by electron collisions is due to the collisional de-trapping of magnetically trapped electrons, which enhance ITG growth rate [23]. All growth rates and real frequencies are summarized in the legends of figures 4(*b*)–(*e*), where real frequencies and growth rates are in units of kHz and krad/s, respectively, and are taken in the lab frame. Also, mode amplitudes are normalized in each panel according to each panel's respective maximum value, as these are linear simulations and the physical value of the amplitude is arbitrary. The relative instability strength of each physics case can be inferred from the difference in growth rates. Figure 4(*f*) shows the perturbed electrostatic potential in a poloidal cross section for the comprehensive case, which is observed to be ballooning.

When including both collisions and $E_r$, GTC simulations (figure 4(*e*)) reveal the linear eigenmodes to be localized near $\psi_N = 0.72$ during ELM suppression–this is not near the region at the top of the pedestal ($\psi_n \approx 0.94$). However, nonlinear simulations in section 4.3 will show a qualitative difference at the top of the pedestal due to turbulence spreading from the region where the linear growth rate peaks at $\psi_n \approx 0.72$ to the top of the pedestal at $\psi_n \approx 0.94$.

### 4.3. Nonlinear spreading

After considering the linear effects of different physics and gaining insight into the roles of collisions and $E_r$, nonlinear simulations, with both collisions and $E_r$, of 158104.01350, 158103.03750, and 158103.03050 are carried out. Figure 5 depicts the radial profiles of simulation inputs and simulation results for all three DIII-D cases. The figure shows the pressure drive and Er shear profiles (top row), radial profiles (flux-surface-averaged) for the linear and nonlinear phases of the fluctuations (middle row), and the observed transport coefficients (bottom row). In all three cases, linear eigenmodes are localized away from the pedestal top ($\psi_N = [0.7, 0.8]$), with those of 158103.03050, during ELM suppression, being slightly broader. Nonlinear spreading of turbulence is observed in all three cases, however, the larger $E \times B$ shearing rate at the top of the pedestal in the ELMing cases prevents the turbulence from spreading past $\psi_N \sim 0.8$. Evidence for actual turbulence spreading is observed, as time histories of the perturbed electrostatic potential at outer radii (beyond $\psi_N \sim 0.8$) show that perturbations in these regions only begin to grow after the turbulence has spread to those regions. In the ELM suppressed case, the $E \times B$ shearing rate is significantly lower between $\psi_N = [0.8, 0.9]$, and the turbulence is observed to spread to $\psi_N = 0.93$, the pedestal top. Similar trends are found in the heat and particle transport coefficient, shown in figures 5(*g*)–(*i*). The weakened $E \times B$ shear in the ELM suppressed case leads to higher transport coefficients at the top of the pedestal relative to the ELMing cases. We note that the large electron to ion heat conductivity ratio is due to the strong enhancement of the ITG-like turbulence due to the trapped electrons, as previously seen in [23]. These results are consistent with experimental observations [10] of increased ion-scale turbulence and transport near the pedestal top during RMP induced ELM suppression.

The 2D poloidal mode structures for the linear and nonlinear simulations for these three cases, are in shown figure 6. The upper row depicts the linear phases, which show interchange modes. The black dashed lines depict the simulation boundaries, and the red curves show the $q = 4$ surface in each case. The lower row presents the nonlinear phases of the GTC simulations. It can be seen that the microturbulence spreads to the $q = 4$ surface only for the ELM suppressed case, and not for the two ELMing cases. The turbulence is shown to spread farther in figure 6(*f*) than 5(*f*), as in the former we perform rms averages over poloidal angle, and in the latter the outer midplane is shown.

Figure 7 shows the linear and nonlinear spectra of poloidal wavenumber for these three cases. It can be seen that there is significant outward spreading of the longer wavelength turbulence in the ELM suppressed case, as the turbulence is observed to spread to the pedestal top, $\psi_N \sim 0.93$ in that case only. The ELMing cases, with and without $n = 2$ RMPs, do not exhibit a strong downward spectral cascade, nor outward spreading, as there is a large $\omega_s$ separating the regions of significant linear instability and the pedestal top.

To demonstrate that the enhanced turbulence spreading in the ELM suppressed case is due to the weaker $E \times B$ shear, nonlinear simulations of shot #158103.03050 have been repeated with the $E \times B$ shear scaled up by a factor of two. Figure 8(*a*) shows the original and doubly scaled $E \times B$ shearing profiles, along with the pressure scale length profile for 158103.03050 in the simulation domain. Figure 8(*b*) shows the new (purple) radial profile of the flux-surface-averaged electrostatic potential. The nonlinear turbulence spreading for the two times $E \times B$ shear is seen to entirely stop near $\psi_N \sim 0.85$, and the mode amplitude between $\psi_N = [0.7, 0.85]$ is significantly less than the original case (red). Thus, we conclude that the turbulence spreading in this RMP ELM suppressed case is due its weak $E \times B$ shearing rate.

## 5. Discussion and conclusion

Nonlinear electrostatic GTC simulations of DIII-D shot 158104 at 1350 ms (ELMing no RMP), 158103 at 3750 ms (ELMing with $n = 2$ RMP), and 158103 at 3050 ms (ELM suppressed with $n = 2$ RMP) find significantly larger and broader turbulence and transport at the pedestal top in the ELM suppressed case. From gyrokinetic simulations, linear eigenmodes, localized in the core, nonlinearly spread to the pedestal top. This increase in turbulence spreading is attributed to the $E_r$ shearing rate being significantly lower just inside of the pedestal top in the ELM suppressed case. These results are consistent with previous observations [10] of significant increases of fluctuations near the pedestal top, and may explain these observations.

Our results suggest that the observed decrease in the $E \times B$ shear near the pedestal top may account for the increase in ion-scale fluctuations observed in these experiments in the transition to ELM suppression. Our GTC simulations also show a significant increase in transport at the top of the pedestal in the ELM suppressed phase, suggesting that the reduction of $E \times B$ shear can contribute to ELM suppression by enhancing turbulent transport at the top of the pedestal. However, demonstrating the physics mechanism behind the $E_r$ profile change during ELM suppression is beyond the scope of this work. Moreover, we note that the increase of ion scale turbulence and decrease in $E \times B$ shear, at the pedestal top, are not universal conditions of ELM suppression, as noted earlier [3, 12]. Hence, our results suggest that pedestal top transport stemming from a reduction of $E \times B$ shear can help limit the pedestal width, but it may not be needed in all cases of RMP induced ELM suppression. Therefore, it is important to increase the experimental database to identify the different physical mechanisms capable of limiting the growth of the pedestal to an unstable width, and achieving RMP induced ELM suppression, as well as developing a predictive model to explain the dependency of the equilibrium radial electric field on the RMP.

## Acknowledgments

This material is based upon work supported by the U.S. Department of Energy (DOE), Office of Science, Office of Fusion Energy Sciences, using the DIII-D National Fusion Facility, a DOE Office of Science user facility, under Awards DE-FC02-04ER54698, DOE grant DE-SC0013804 and SciDAC ISEP. Part of this work was performed under the auspices of the U.S. Department of Energy by Lawrence Livermore National Laboratory under Contract DE-AC52-07NA27344, and by Princeton Plasma Physics Laboratory under Contract DE-AC02-09CH11466. DIII-D data shown in this paper can be obtained in digital format by following the links at https://fusion.gat.com/global/D3D_DMP.

## Disclaimer

## ORCID iDs

D. Spong https://orcid.org/0000-0003-2370-1873

## References

[1] Lang P. *et al* 2013 ELM control strategies and tools: status and potential for ITER *Nucl. Fusion* **53** 043004
[2] Evans T. *et al* 2005 Suppression of large edge localized modes in high confinement DIII-D plasmas with a stochastic magnetic boundary *J. Nucl. Mater.* **337** 691–6
[3] McKee G. *et al* 2013 Increase of turbulence and transport with resonant magnetic perturbations in ELM-suppressed plasmas on DIII-D *Nucl. Fusion* **53** 113011
[4] Wade M. *et al* 2015 Advances in the physics understanding of ELM suppression using resonant magnetic perturbations in DIII-D *Nucl. Fusion* **55** 023002
[5] Liang Y. *et al* 2007 Active control of type-I edge-localized modes with $n = 1$ perturbation fields in the jet tokamak *Phys. Rev. Lett.* **98** 265004
[6] ASDEX Upgrade Team *et al* 2011 First observation of edge localized modes mitigation with resonant and nonresonant magnetic perturbations in ASDEX upgrade *Phys. Rev. Lett.* **106** 225004
[7] Jeon Y. *et al* 2012 Suppression of edge localized modes in high-confinement KSTAR plasmas by nonaxisymmetric magnetic perturbations *Phys. Rev. Lett.* **109** 035004
[8] Kirk A. *et al* 2011 Magnetic perturbation experiments on MAST L-and H-mode plasmas using internal coils *Plasma Phys. Control. Fusion* **53** 065011
[9] Snyder P. *et al* 2012 The eped pedestal model: extensions, application to ELM-suppressed regimes, and ITER predictions *Proc. 24th IAEA Fusion Energy Conf. (San Diego, CA)*
[10] Nazikian R. *et al* 2015 Pedestal bifurcation and resonant field penetration at the threshold of edge-localized mode suppression in the DIII-D tokamak *Phys. Rev. Lett.* **114** 105002
[11] Paz-Soldan C. *et al* 2016 Optimization of the plasma response for the control of edge-localized modes with 3D fields *Proc. 26th IAEA Fusion Energy Conf. (Kyoto, Japan)*
[12] Moyer R.A. *et al* 2017 Validation of the model for ELM suppression with 3D magnetic fields using low torque ITER baseline scenario discharges in DIII-D *Phys. Plasmas* **24** 102501
[13] Lin Z., Hahm T.S., Lee W., Tang W.M. and White R.B. 1998 Turbulent transport reduction by zonal flows: massively parallel simulations *Science* **281** 1835–7
[14] Xiao Y., Holod I., Wang Z., Lin Z. and Zhang T. 2015 Gyrokinetic particle simulation of microturbulence for general magnetic geometry and experimental profiles *Phys. Plasmas* **22** 022516
[15] Holod I., Lin Z., Taimourzadeh S., Nazikian R., Spong D. and Wingen A. 2016 Effect of resonant magnetic perturbations on microturbulence in DIII-D pedestal *Nucl. Fusion* **57** 016005
[16] Zhu W. *et al* 2006 Observation of plasma toroidal-momentum dissipation by neoclassical toroidal viscosity *Phys. Rev. Lett.* **96** 225002
[17] Joseph I. 2012 Edge-localized mode control and transport generated by externally applied magnetic perturbations *Contrib. Plasma Phys.* **52** 326–47
[18] Burrell K. 1997 Effects of $E \times B$ velocity shear and magnetic shear on turbulence and transport in magnetic confinement devices *Phys. Plasmas* **4** 1499–518
[19] Lin Z. and Hahm T. 2004 Turbulence spreading and transport scaling in global gyrokinetic particle simulations *Phys. Plasmas* **11** 1099–108
[20] Fulton D., Lin Z., Holod I. and Xiao Y. 2014 Microturbulence in DIII-D tokamak pedestal. I. Electrostatic instabilities *Phys. Plasmas* **21** 042110
[21] Liao X., Lin Z., Holod I., Xiao Y., Li B. and Snyder P. 2016 Microturbulence in DIII-D tokamak pedestal. III. Effects of collisions *Phys. Plasmas* **23** 122507
[22] Liao X., Lin Z., Holod I., Li B. and Sun G. 2016 Microturbulence in DIII-D tokamak pedestal. IV. Electrostatic turbulent transport *Phys. Plasmas* **23** 122305
[23] Lin Z., Nishimura Y., Xiao Y., Holod I., Zhang W. and Chen L. 2007 Global gyrokinetic particle simulations with kinetic electrons *Plasma Phys. Control. Fusion* **49** B163

[24] Bao J., Liu D. and Lin Z. 2017 A conservative scheme of drift kinetic electrons for gyrokinetic simulation of kinetic-MHD processes in toroidal plasmas *Phys. Plasmas* **24** 102516

[25] Lee W. 1983 Gyrokinetic approach in particle simulation *Phys. Fluids* **26** 556–62

[26] Brizard A. and Hahm T. 2007 Foundations of nonlinear gyrokinetic theory *Rev. Mod. Phys.* **79** 421

[27] Lee W. 1987 Gyrokinetic particle simulation model *J. Comput. Phys.* **72** 243–69

[28] Horton W. 1999 Drift waves and transport *Rev. Mod. Phys.* **71** 735

[29] Holod I. and Lin Z. 2013 Verification of electromagnetic fluid-kinetic hybrid electron model in global gyrokinetic particle simulation *Phys. Plasmas* **20** 032309

[30] Paz-Soldan C. *et al* 2015 Observation of a multimode plasma response and its relationship to density pumpout and edge-localized mode suppression *Phys. Rev. Lett.* **114** 105001

[31] Hirshman S. and Whitson J. 1983 Steepest-descent moment method for three-dimensional magnetohydrodynamic equilibria *Phys. Fluids* **26** 3553–68